Supplement of Atmos. Chem. Phys., 17, 14975–14985, 2017
https://doi.org/10.5194/acp-17-14975-2017-supplement

Atmospheric Chemistry and Physics
Open Access
EGU

Supplement of

The single-particle mixing state and cloud scavenging of black carbon: a case study at a high-altitude mountain site in southern China

Guohua Zhang et al.

Correspondence to: Xinhui Bi (bixh@gig.ac.cn)

SPAMS

Individual particles are introduced into SPAMS through a critical orifice. They are focused and accelerated to specific velocities, determined by two continuous diode Nd:YAG laser beams (532 nm), which are used to trigger a pulsed laser (266 nm) to desorp/ionize the particles. The produced positive and negative molecular fragments are recorded. In summary, a velocity, a detection moment, and an ion mass spectrum are recorded for each ionized particle, while there is no mass spectrum for not ionized particles. The velocity could be converted to d_{va} based on a calibration using polystyrene latex spheres (PSL, Duke Scientific Corp., Palo Alto) with predefined sizes. The accuracy for the derived d_{va} is within ±10%.

Aethalometer data analysis

The absorption coefficients at seven different wavelengths (370, 450, 520, 590, 660, 880 and 950 nm) were obtained by the Aethalometers. A variable attenuation (ATN), is defined to represent the filter attenuation through the sample spot on a filter (Weingartner et al., 2003; Arnott et al., 2005; Backman et al., 2016). It is well known that the measured ATN may differ from the true aerosol absorption due to 'filter loading effect', a phenomenon which appears as a gradual decrease of instrumental response as the aerosol loading on the filter increases (Arnott et al., 2005). Therefore, two calibration factors are introduced to convert aethalometer attenuation measurements to "real" absorption coefficient (Weingartner et al., 2003). At 880 nm wavelength, light absorption can be attributed to BC alone rather than the other aerosol particles due to their significantly less absorption at long wavelength (e.g., Sandradewi et al., 2008; Yang et al., 2009). For AE–31, a specific attenuation cross-section σ_{ATN} of 16.6 $m^2\ g^{-1}$, recommended by the manufacturer, was applied to calculate the EBC concentration with the equation: EBC = b_{ATN}/σ_{ATN}, where b_{ATN} is the optical attenuation coefficient. For AE-33, the ATN was converted to an EBC concentration using the mass absorption cross section of 7.77 $m^2\ g^{-1}$ according to the method recommended by Drinovec et al. (2015).

The AE-31 used in the present study may suffer from the effects described above. Differently, the AE-33 has been improved by the incorporation of a filter loading correction part, based on a two parallel spot measurement of optical absorption. It could provide a real-time output of the "loading compensation" parameter to compensate for the "loading effect". The details of the principle of operation, data deduction, and error budget of the AE-33, the inherent uncertainties in its technique and the corrections are extensively available in the literature (Drinovec et al., 2015). Therefore, we reported EBC concentration from the results of AE-33. The detection limit for EBC measurements is < 10 ng m^{-3} with uncertainty at ~2 ng m^{-3} at the time-base of 1 minute (http://www.mageesci.com/). As noted in the manuscript and Fig. S10, the EBC measured by AE-31 is significantly correlated ($R^2 = 0.9$, $p < 0.001$) with that measured by AE-33. Therefore, EBC concentrations derived from AE-31 were not corrected for the calculation of $Mf_{scav,EBC}$.

As shown in Fig. S10, AE-31 might underestimate ~15% of EBC for cloud INT particles in the calculation of $Mf_{scav,EBC}$. It is also noted that a threshold of 8 μm might underestimate the mass concentration of cloud RES EBC, since the size of droplets might extend to as low as 3 μm. Unfortunately, the size distribution of cloud droplets was not available for our study. Therefore, we assumed that the largest underestimate of the cloud RES particles is 30% to assess the uncertainties for $Mf_{scav,EBC}$ calculation. The mean $Mf_{scav,EBC}$ was recalculated to be 30-36%, when the assumed largest underestimate (i.e., 30%) of the cloud RES particles and ~15% underestimate of the cloud INT BC were taken into account in R1. Compared to mean $Mf_{scav,EBC}$ = 33%, the overall uncertainties for the estimate of mean $Mf_{scav,EBC}$ is with 10%.

69 Table S1. Average mass concentrations, mass fractions relative to fine particles and scavenged fractions of BC from the literatures.

Site	site type	season (year)	ave (± std) ($\mu g\ m^{-3}$)	mass fraction	$Mf_{scav,EBC}$ (%)	References
Shenzhen, Southern China	urban	Summer (2011)	4.0 ± 3.1	~11%	-[a]	(Lan, et al., 2013)
Guangzhou, Southern China	urban	Summer (2008)	8.86	-	-	(Wu, et al., 2013)
Guangzhou, Southern China	urban	Fall(2010)	4.3	~4%[b]	-	(Zhang, et al., 2013)
Shenzhen, Southern China	urban	Fall(2009)	6.0 ± 6.3	-	-	(Huang, et al., 2012)
Guangzhou, Southern China	Rural	Summer (2008)	2.62	-	-	(Wu, et al., 2013)
Ba Guang village, southern China	Rural	Fall(2009)	2.6 ± 1.0	-	-	(Huang, et al., 2012)
Mt. Soledad (251 m m.s.l.)	marine	Summer (2012)	0.07	-	-	(Schroder, et al., 2015)
Yongxing Island, Southern China	marine	Summer (2008)	0.54	-	-	(Wu, et al., 2013)
A coastal Chilean hill, (Valparaíso), 450 m a.s.l.	low-altitude	Winter (2013)	0.34 - 0.95	-	13 - 50	(Hitzenberger et al., 2016)
Puy de Dome (France), 1465 m a.s.l.	mid-altitude	Winter-spring (2001)	-	-	33 - 74	(Sellegri et al., 2003)
Nova Scotia, Canada (Below 1 km)	mid-altitude	Summer (1993)	0.06 ± 0.01	-	2 - 32	(Chylek et al., 1996)

Nova Scotia, Canada (1-3 km)	mid-high-altitude	Summer (1993)	0.22 ± 0.03	-	-	(Chylek et al., 1996)
Mt. Rax (1644 m a.s.l.)	high-altitude	Spring (1999)	0.43	-	-	(Hitzenberger et al., 2001)
Mt. Rax (1644 m a.s.l.)	high-altitude	Spring (2000)	0.72	-	54 ± 25	(Hitzenberger et al., 2001)
Alpine Jungfraujoch (Switzerland), 3850 m a.s.l.	high-altitude	Summer (2004)	0.06	-	61	(*Cozic et al.*, 2007)
Alpine Jungfraujoch (Switzerland), 3850 m a.s.l.	high-altitude	Winter (2004)	0.05	-	-	(*Cozic et al.*, 2007)

[a] not available.

[b] mass fraction relative to PM_3.

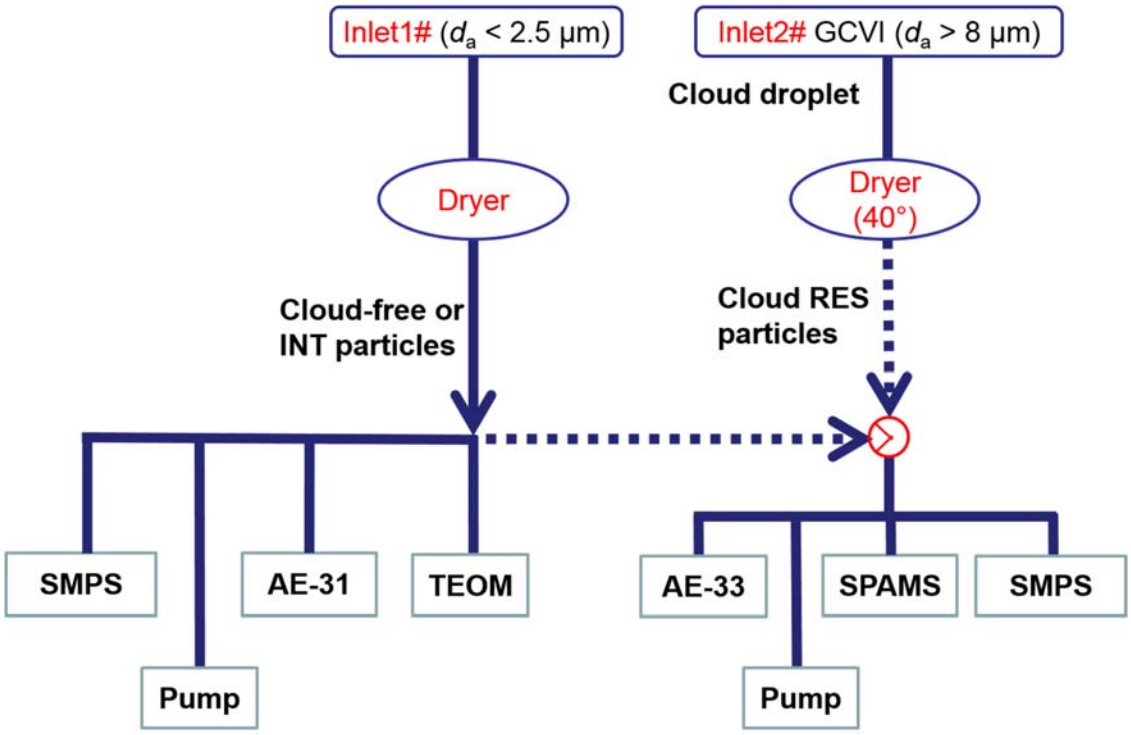

Figure S1. A scheme of the instrumentation setup in this study. The dash line illustrates that the sampling pipe was either connected to Inlet 1# or Inlet 2#. As described in section 2.1, the cloud INT and RES particles were intermittently measured by these instruments during Cloud III, through manually connect the sampling pipe to either Inlet 1# or Inlet 2# at approximately one-hour intervals. The GCVI includes various sensors to monitor the temperature/RH, visibility (http://belfortinstrument.com/products/all-environment-visibility-sensor/), and rainfall/snow (http://www.meltyourice.com/products/controllers/ds-82/). The integrated rainfall/snow sensor helps to exclude sampling during rainy periods. TEOM (https://www.thermofisher.com) measures the mass concentration of aerosol with the detection limited of ~100 ng m^{-3}, with an accuracy of ±0.75%. MSP SMPS (https://www.mspcorp.com) measures the number-based size distribution of particles

ranged between 10-1000 nm in 48 size bins, with a detection limit of ~1 cm^{-3}, and an accuracy of ±10%. Grimm SMPS (https://www.mspcorp.com) can measure the number-based size distribution of particles ranged between 10-1100 nm in 44 size bins, with a detection limit of ~1 cm^{-3}, and an accuracy of ±5%.

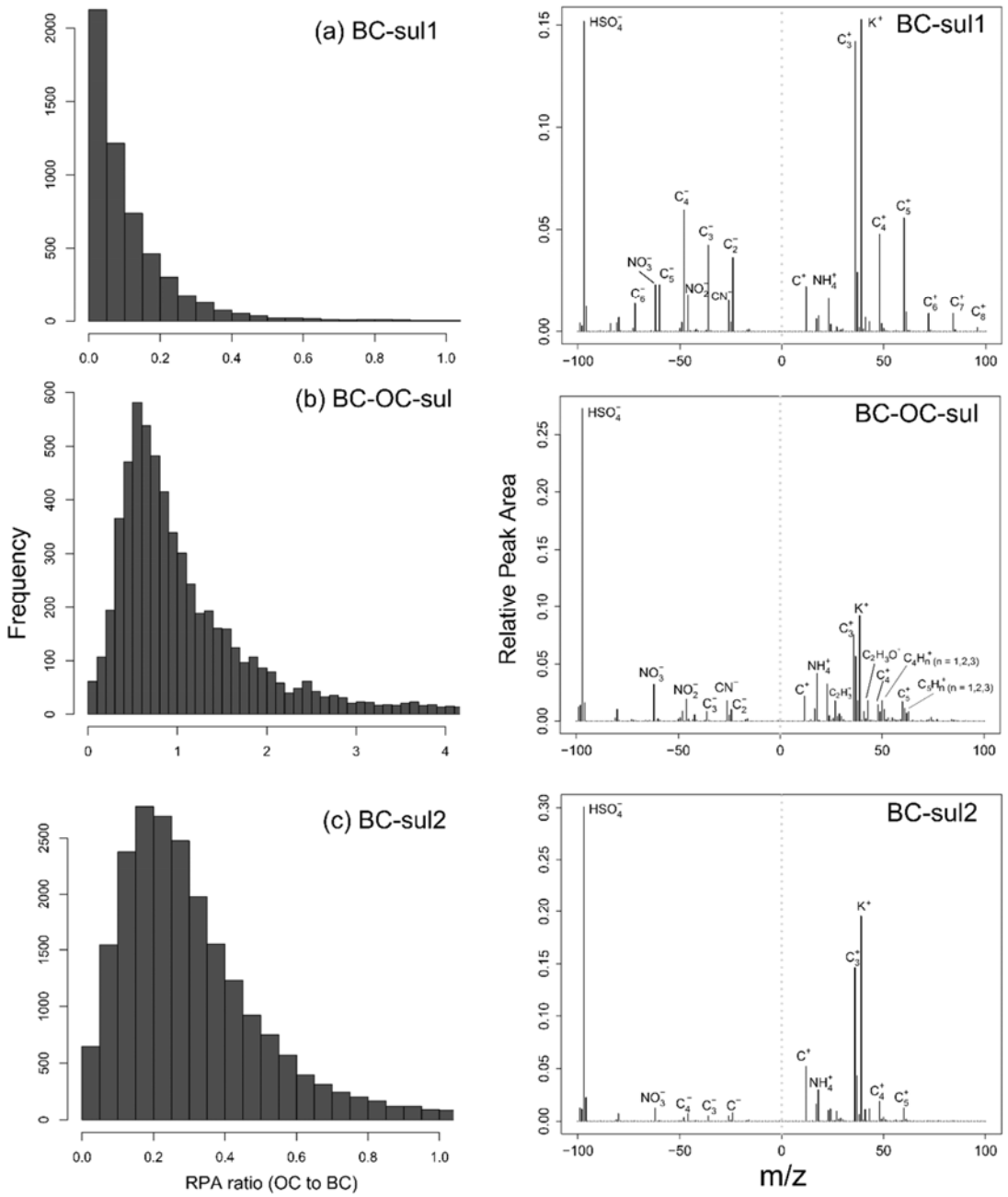

90

91 **Figure S2.** Statistic analysis on the RPA ratio of OC to BC (left), and the average mass

92 spectra (right) for the BC types. Markers were selected as m/z 27, 43, 50, 51, 61, 63, -26

93 for OC, and carbon ion clusters ($C_n^{+/-}$, $n \leq 5$) for BC, the same as those in Fig. 3. More

94 intense sulfate (RPA = ~0.3) was found for BC-sul2 and BC-OC-sul, relative to that

(RPA = ~0.15) for BC-sul1 type. More abundance of OC was found for BC-OC-sul, the mean peak area ratio OC/BC of which is ~1, higher than those (< 0.3) for other BC types.

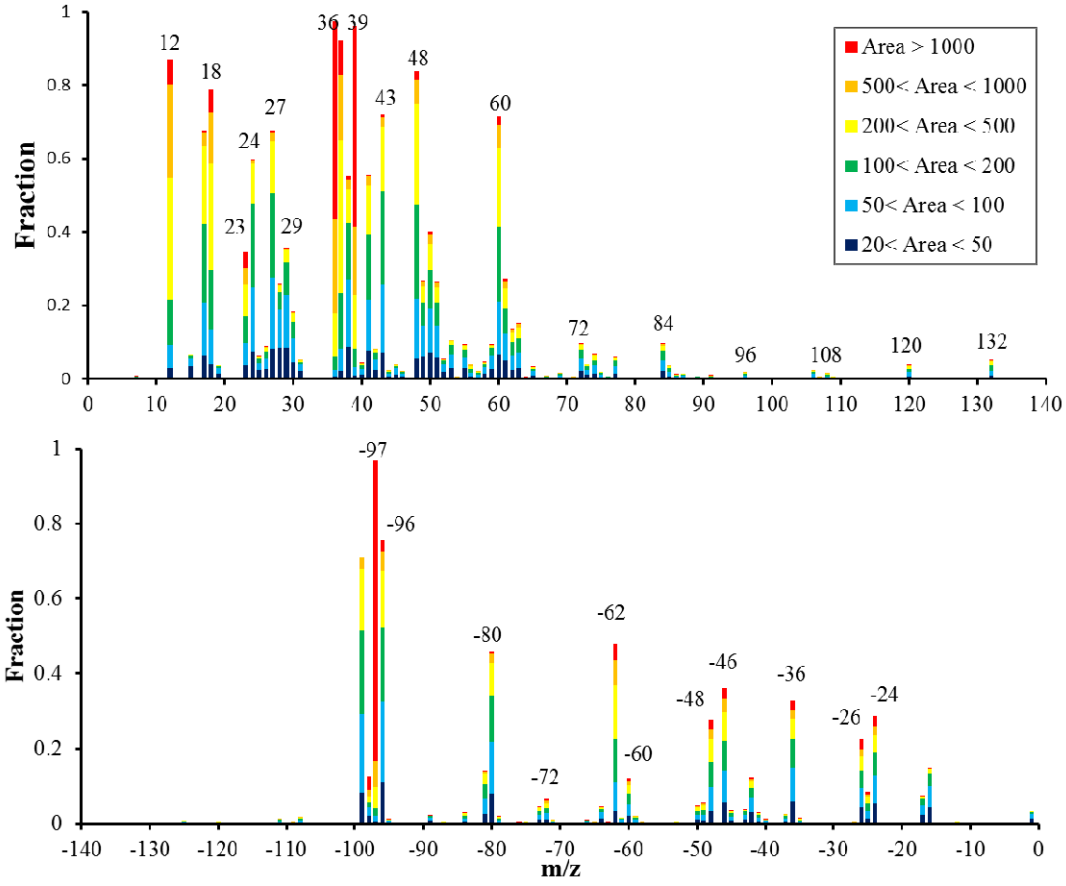

Figure S3. The number-based digitized mass spectrum of cloud-free BC-containing particles at the remote high-altitude site. Y-axis indicates the number fraction of total particles that had detectable amounts of these individual ion peaks.

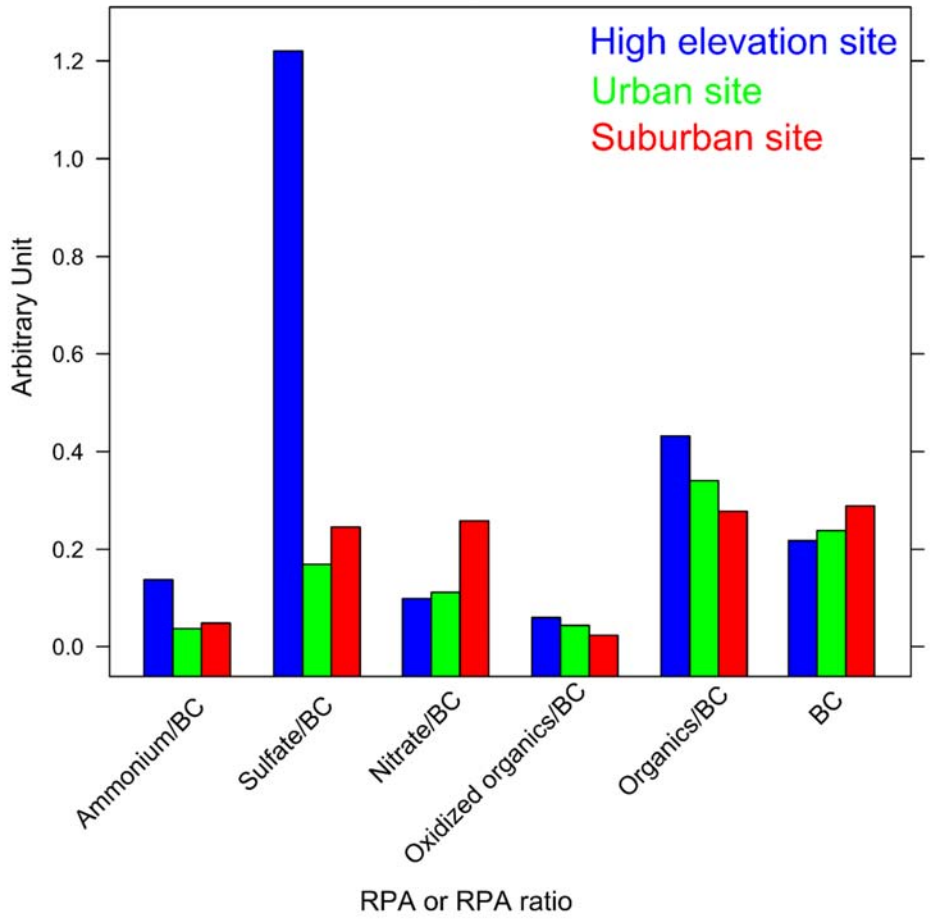

101

102 Figure S4. RPA ratio of ammonium (m/z 18), sulfate (m/z -97), nitrate (m/z -62),
103 oxidized organics (m/z 43), and other organics (m/z 27, 50, 51, 61, 63, -26) to BC, and
104 RPA of BC (carbon ion clusters ($C_n^{+/-}$, $n \leq 5$)) at the high elevation site, urban
105 (Guangzhou), and suburban sites (Heshan) during winter in southern China. The particles
106 in Guangzhou and Heshan were similarly measured by SPAMS during winter. Despite of
107 matrix effects due to the laser desorption/ionization for SPAMS, advances have been
108 made in semi-quantifying individual chemical species, either through multivariate
109 analysis or by applying peak intensities for specific ions (e.g., Jeong et al., 2011; Xing et
110 al., 2011; Healy et al., 2013). RPA, defined as the peak area of each m/z divided by the

111 total dual ion mass spectral peak area, is related to the relative amount of a species on a
112 particle. Compared to absolute peak area, RPA was commonly applied because it is less
113 sensitive to the variability in ion intensities associated with particle-laser interactions. It
114 is also noted that matrix effects might be lower when calculation was performed for
115 similar particle type, i.e., BC-containing particles.

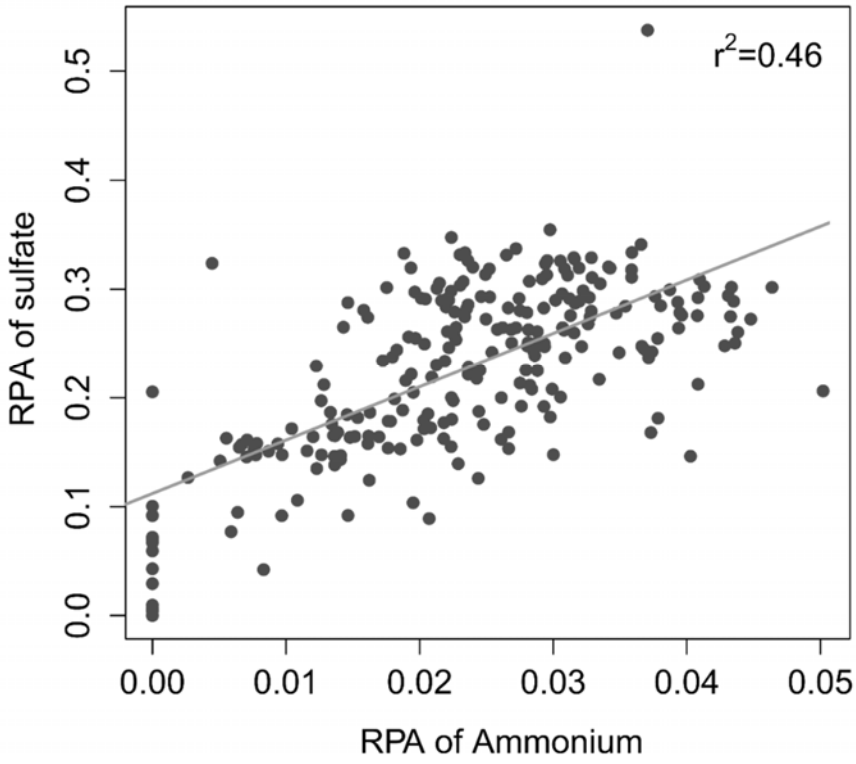

116

117 Figure S5. Correlation analysis of hourly average RPA for ammonium and sulfate
118 associated with BC-containing particles. The correlation coefficient is a bit lower than
119 expected might partly due to matrix effect in single particle mass spectrometry (e.g.,
120 Jeong et al., 2011; Xing et al., 2011; Healy et al., 2013).

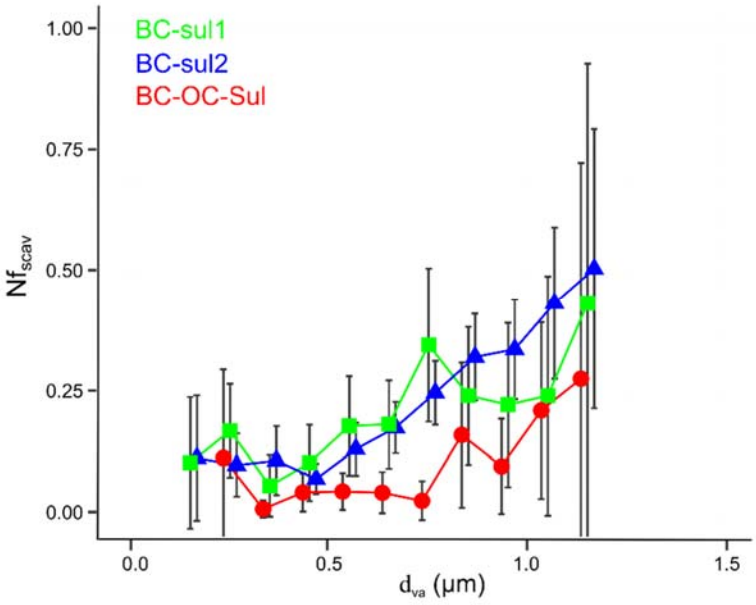

121

122 Figure S6. Size-resolved Nf_{act} estimated for three particle types of BC-containing
123 particles. Note that this data only collected during Cloud III event when both cloud RES
124 and INT particles were collected, however, not simultaneously but intermittently. It is
125 noted that although the Nf_{act} for BC-OC-sul type is lower than BC-sul types, the Nf_{act} for
126 all the BC-containing particles is similar to that of all the detected particles. We attributed
127 it to two reasons: (1) BC-OC-sul particles only accounted for ~20% of BC-containing
128 particles, and (2) the other particles also contained OC-dominated particles (~10%).

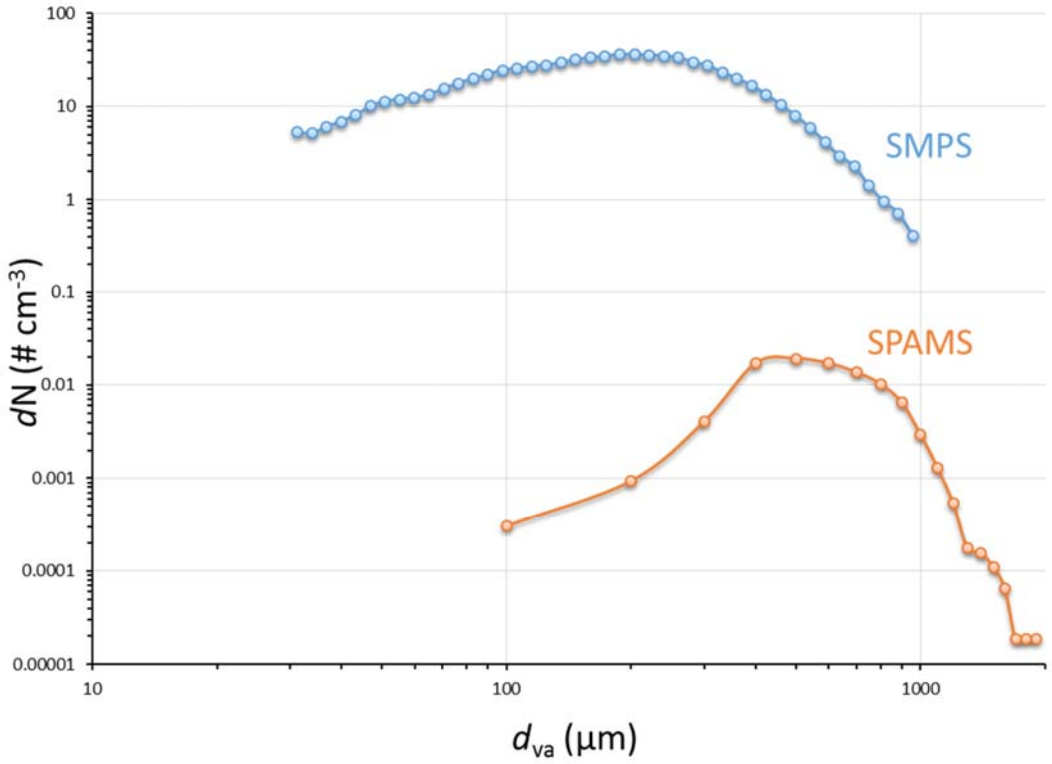

129

130 Figure S7. A representative comparison between the size distributions measured by the
131 SPAMS and the SMPS within 12 hours measurements. It should be noted that the
132 diameter is represented as d_{va} by SPAMS, while the diameter measured by the SMPS is
133 represented as electrical mobility diameter (d_m). Herein, the d_m was first converted to the
134 d_{va} for the comparison. The conversion could be simplified to $d_m = d_{va} * \rho_{eff}/\rho_0$ (DeCarlo et
135 al., 2004), where ρ_{eff} refers to the effective density, ρ_0 is the unit density 1.0 g cm^{-3}. The
136 ρ_{eff} is assumed to be 1.5 g cm^{-3} for the calculation (Hu et al., 2012).

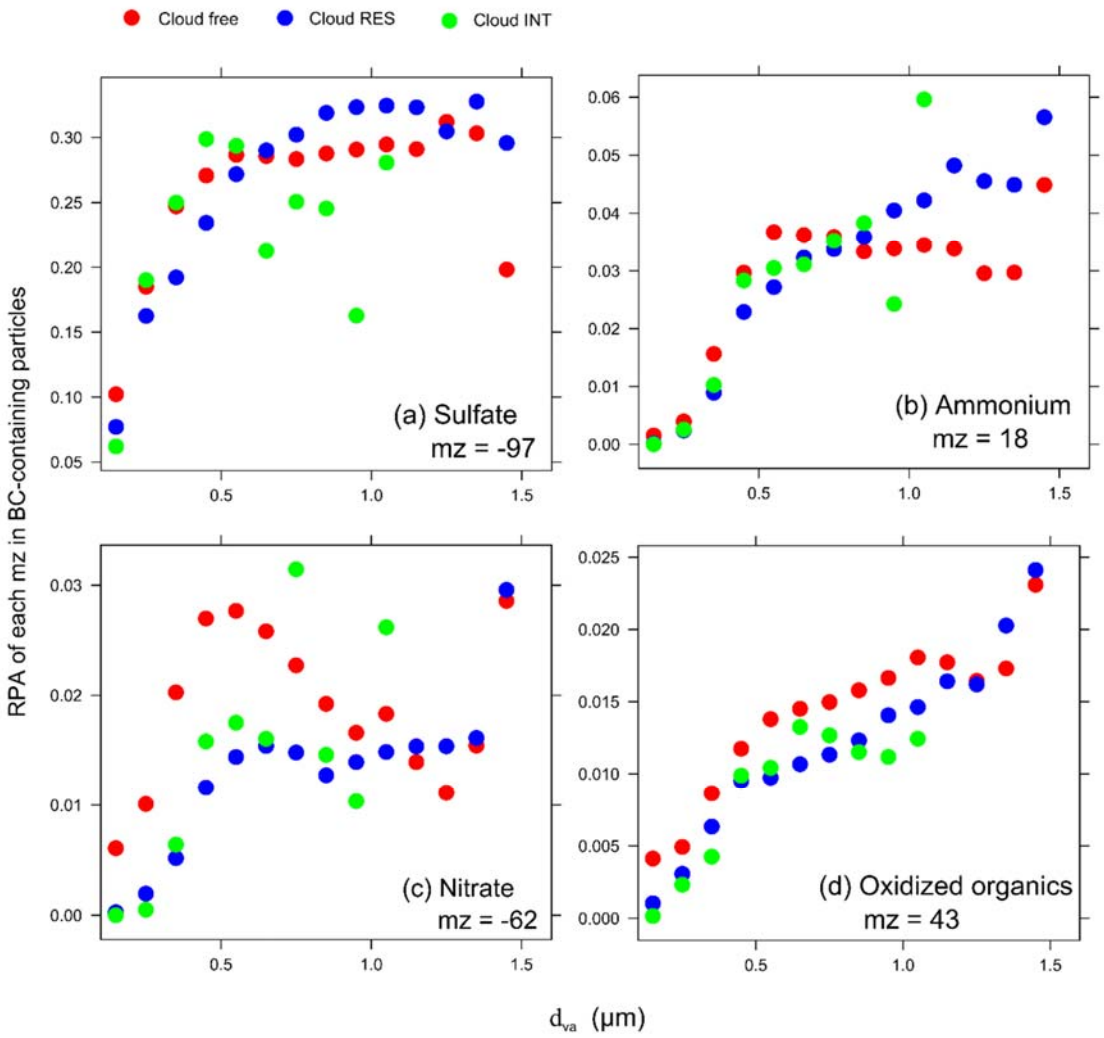

137

138 Figure S8. RPA of each secondary species associated with BC-containing particles in

139 cloud-free, INT, and RES particles as a function of particle sizes.

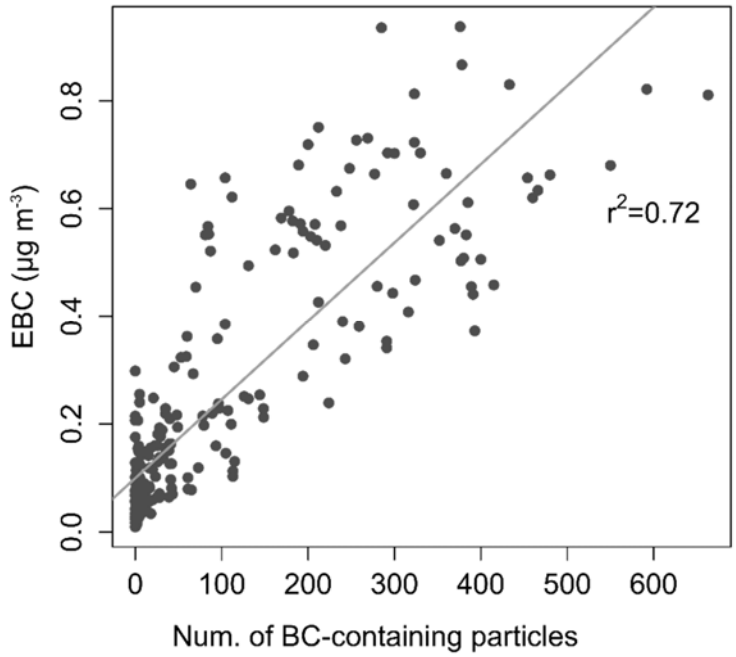

140

141 Figure S9. Correlation between time series of Num. of BC-containing particles and
142 concentration of EBC. The volume equivalent diameter of BC particles cores measured in
143 southern China was typically around 200 nm (Huang et al., 2011; Huang et al., 2012).
144 Huang et al. (2011) showed that a large fraction (> 60%) of BC particles are internally
145 mixed with a significant amount of non-refractory materials (coating thickness > 70 nm)
146 at a rural site in southern China. Furthermore, Yu et al. (2010) showed that over 50% of
147 BC are above 500 nm, also indicating internally mixed of BC, with regard that majority of
148 BC particles cores have volume equivalent diameter less than 500 nm (Huang et al., 2011;
149 Huang et al., 2012). As also discussed in section 3.1, BC-containing particles were already
150 heavily mixed with secondary species arriving at our site, and therefore they should be
151 larger enough for the detection by SPAMS.

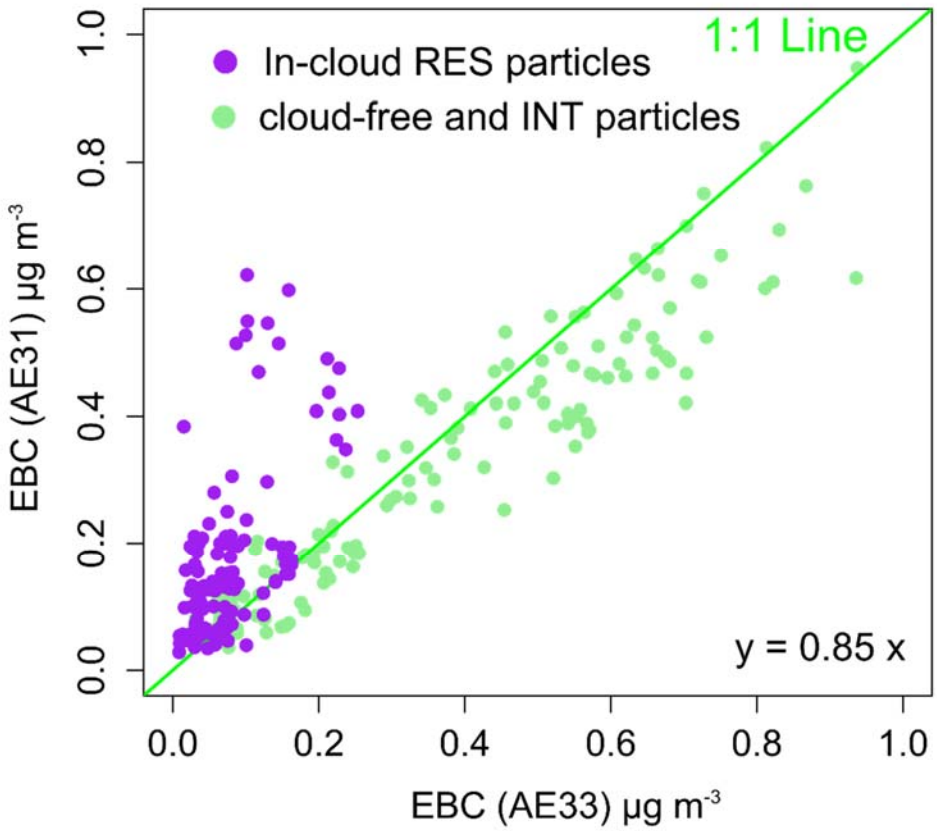

152

153 Figure S10. Correlation analysis of EBC measured by AE31 and AE33. They measured
154 the same aerosol for out-of-cloud (including cloud INT and cloud-free) particles. However,
155 during cloud events, AE33 measured cloud RES particles or cloud INT particles for some
156 periods, while AE31 measured cloud INT particles. Therefore, the EBC were compared
157 when the same aerosol were measured, as shown in green dots. The result indicates that
158 they are highly correlated, with EBC measured by AE31 only slightly lower than those by
159 AE33.

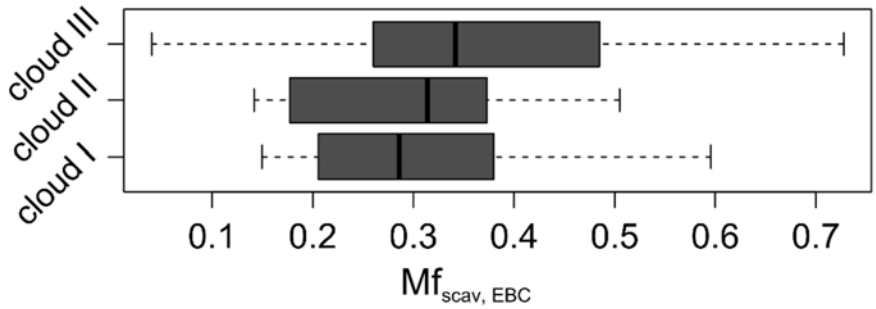

160

161 Figure S11. Box and whisker plot of $Mf_{scav,EBC}$ for each cloud event. In a box and whisker
162 plot, the lower, median and upper lines of the box denote the 25th, 50th, and 75th
163 percentiles, respectively, and the lower and upper edges of the whisker denote the 10th
164 and 90th percentiles, respectively.

165 Reference

166 Arnott, W. P., Hamasha, K., Moosmuller, H., Sheridan, P. J., and Ogren, J. A.: Towards
167 aerosol light-absorption measurements with a 7-wavelength Aethalometer:
168 Evaluation with a photoacoustic instrument and 3-wavelength nephelometer, Aerosol
169 Sci. Tech., 39, 17-29, doi:10.1080/027868290901972, 2005.
170 Backman, J., Schmeisser, L., Virkkula, A., Ogren, J. A., Asmi, E., Starkweather, S.,
171 Sharma, S., Eleftheriadis, K., Uttal, T., Jefferson, A., Bergin, M., and Makshtas, A.:
172 On Aethalometer measurement uncertainties and multiple scattering enhancement in
173 the Arctic, Atmos. Meas. Tech. Discuss., 2016, 1-31, doi:10.5194/amt-2016-294,
174 2016.
175 DeCarlo, P. F., Slowik, J. G., Worsnop, D. R., Davidovits, P., and Jimenez, J. L.: Particle
176 morphology and density characterization by combined mobility and aerodynamic
177 diameter measurements. Part 1: Theory, Aerosol Sci. Tech., 38, 1185-1205,
178 doi:10.1080/027868290903907, 2004.
179 Drinovec, L., Močnik, G., Zotter, P., Prévôt, A. S. H., Ruckstuhl, C., Coz, E., Rupakheti,
180 M., Sciare, J., Müller, T., Wiedensohler, A., and Hansen, A. D. A.: The "dual-spot"
181 Aethalometer: an improved measurement of aerosol black carbon with real-time
182 loading compensation, Atmos. Meas. Tech., 8, 1965-1979, doi:10.5194/amt-8-1965-
183 2015, 2015.
184 Healy, R. M., Sciare, J., Poulain, L., Crippa, M., Wiedensohler, A., Prevot, A. S. H.,
185 Baltensperger, U., Sarda-Esteve, R., McGuire, M. L., Jeong, C. H., McGillicuddy, E.,
186 O'Connor, I. P., Sodeau, J. R., Evans, G. J., and Wenger, J. C.: Quantitative
187 determination of carbonaceous particle mixing state in Paris using single-particle
188 mass spectrometer and aerosol mass spectrometer measurements, Atmos. Chem.
189 Phys., 13, 9479-9496, doi:10.5194/acp-13-9479-2013, 2013.
190 Huang, X. F., Gao, R. S., Schwarz, J. P., He, L. Y., Fahey, D. W., Watts, L. A.,
191 McComiskey, A., Cooper, O. R., Sun, T. L., Zeng, L. W., Hu, M., and Zhang, Y. H.:
192 Black carbon measurements in the Pearl River Delta region of China, J. Geophys.
193 Res., 116, 445-451, doi:10.1029/2010jd014933, 2011.
194 Huang, X. F., Sun, T. L., Zeng, L. W., Yu, G. H., and Luan, S. J.: Black carbon aerosol

characterization in a coastal city in South China using a single particle soot photometer, Atmos. Environ., 51, 21-28, doi:10.1016/j.atmosenv.2012.01.056, 2012.

Jeong, C. H., McGuire, M. L., Godri, K. J., Slowik, J. G., Rehbein, P. J. G., and Evans, G. J.: Quantification of aerosol chemical composition using continuous single particle measurements, Atmos. Chem. Phys., 11, 7027-7044, doi:10.5194/acp-11-7027-2011, 2011.

Sandradewi, J., Prevot, A. S. H., Szidat, S., Perron, N., Alfarra, M. R., Lanz, V. A., Weingartner, E., and Baltensperger, U.: Using aerosol light absorption measurements for the quantitative determination of wood burning and traffic emission contributions to particulate matter, Environ. Sci. Technol., 42, 3316-3323, 2008.

Weingartner, E., Saathoff, H., Schnaiter, M., Streit, N., Bitnar, B., and Baltensperger, U.: Absorption of light by soot particles: determination of the absorption coefficient by means of aethalometers, J. Aerosol Sci., 34, 1445-1463, doi:http://dx.doi.org/10.1016/S0021-8502(03)00359-8, 2003.

Xing, J. H., Takahashi, K., Yabushita, A., Kinugawa, T., Nakayama, T., Matsumi, Y., Tonokura, K., Takami, A., Imamura, T., Sato, K., Kawasaki, M., Hikida, T., and Shimono, A.: Characterization of Aerosol Particles in the Tokyo Metropolitan Area using Two Different Particle Mass Spectrometers, Aerosol Sci. Tech., 45, 315-326, doi:10.1080/02786826.2010.533720, 2011.

Yang, M., Howell, S. G., Zhuang, J., and Huebert, B. J.: Attribution of aerosol light absorption to black carbon, brown carbon, and dust in China - interpretations of atmospheric measurements during EAST-AIRE, Atmos. Chem. Phys., 9, 2035-2050, 2009.

Yu, H., Wu, C., Wu, D., and Yu, J. Z.: Size distributions of elemental carbon and its contribution to light extinction in urban and rural locations in the pearl river delta region, China, Atmos. Chem. Phys., 10, 5107-5119, doi:10.5194/acp-10-5107-2010, 2010.